

A Spectroscopic Modelling Method for the Detached Eclipsing Binaries to Derive Atmospheric Parameters

Xiang-Lei Chen^{1,2}, A-Li Luo^{1,2,3,4*}, Jian-Jun Chen^{1,2**}, Rui Wang¹, Xiao-Bin Zhang^{1,2}, Wen Hou¹, Bo Qiu⁴, and Fang Zuo¹

¹ CAS Key Laboratory of Optical Astronomy, National Astronomical Observatories, Beijing 100101, China.

² School of Astronomy and Space Science, University of Chinese Academy of Sciences, Beijing 100049, China

³ School of Information Management & Institute for Astronomical Science, Dezhou University, Dezhou 253023, China

⁴ School of Electronic Information Engineering, Hebei University of Technology, Tianjin 300401, China

Received March 7, 2022; accepted March 00, 0000

ABSTRACT

Based on luminosity contributions, we develop a spectroscopic modelling method to derive atmospheric parameters of component stars in binary systems. The method is designed for those spectra of binaries which show double-lined features due to the radial velocities differences between the component stars. We first derive the orbital parameters and the stellar radii by solving the light and radial velocity curves. Then the luminosity contributions in different phases can be calculated. The synthesised double-lined spectra model is constructed by superposing theoretical single-star spectra according to the luminosity contributions. Finally, we derive the atmospheric parameters of each component star by the model fitting method. For multi-epoch double-lined spectra observed by the Large sky Area Multi-Object Spectroscopic Telescope (LAMOST) Medium Resolution Survey ($R \sim 7500$), our method gives robust results for detached eclipsing binary systems observed in different orbital phases. Furthermore, this method can also be applied to other spectroscopic data with different resolutions as long as the systems are detached eclipsing binaries with nearly spherical stars.

Key words. methods: data analysis – (stars:) binaries: spectroscopic – (stars:) binaries: eclipsing

1. Introduction

The binary stars play an important role in the study of stellar evolution. At formation time, stars are always in clusters. In their main sequence time, stars are fractionally in binary systems, depending on their spectral types. Raghavan et al. (2010) considered the fraction is larger than 50% for FGK stars. Duchêne & Kraus (2013) demonstrated that the stellar binarity could be 20% to 80% for different spectral types. By analysing binary stars, stellar structure and evolution can be constrained (Han et al. (2020)). For example, Izzard et al. (2009) gave constraints on the mass of stars that have efficient third dredge up by comparing the observed Carbon-enhanced metal-poor (CEMP) stars with the binary population synthesis (BPS) study results. Another important objects are the Type Ia supernovae (SNe Ia). As classical cosmological distance tracers, the formation channels of SNe Ia affect the Hubble constant measurement and related cosmological assumptions and theories. Traditionally, the binary system consisting of a carbon-oxygen white dwarf and a main sequence/giant/helium donor star was thought to be a progenitor of an SNe Ia (Hoyle & Fowler (1960); Whelan & Iben (1973)). During the later studies, Iben & Tutukov (1984); Webbink (1984); Han (1998) proposed the double degenerate scenario that two carbon-oxygen white dwarfs merging may also cause the explosion of an SNe Ia. Besides the stellar evolution, the binary interaction can change the galaxy spectral energy dis-

tribution (SED). Han et al. (2007) found that the radiation of hot subdwarfs, which are the evolution results of binary interactions, cause the far-ultraviolet excess in the early-type galaxy spectra. Chen et al. (2015) proposed that the galaxy soft X-ray emissions come from the white dwarf accretion in binary systems. The study of binary stars will also contribute to our understanding of the early evolution of the Universe. The hypothesis about the re-ionising photons is that they come from massive single stars. But the photon number is several times less than the required number. Due to the high proportion of binarity of the massive stars, Göteborg et al. (2020) and Secunda et al. (2020) believed that the ionising photons produced by massive binary stars have an important impact on the re-ionisation process in the early Universe.

Depending on whether the mass transfer between the component stars has started, binary systems are divided into detached, semi-detached and contact binaries. This work concentrates on the detached binaries. Detailed analysis of the component stars' characteristics at this stage can not only help to understand the formation of binary stars but also limit the later evolution of mass transfer. Besides mass transfer, the inclination of the orbit is another factor affecting the shape of the light curve. If the inclination of the orbital plane is close to 90° , a binary system is observed as an eclipsing binary star in time domain photometry. Orbital parameters of the eclipsing binaries can be calculated using both the light curve and the radial velocity curve data. And if the orbital period of the binary is shorter than five years, the system can be spectroscopically identified (El-Badry

* A-Li Luo email: lal@nao.cas.cn

** Jian-Jun Chen email: jjchen@nao.cas.cn

et al. (2018)). The orbit of the component stars around each other causes the relative change of radial velocities. The binary spectra thus show double-peaked features and they are called ‘SB2’ spectra. One can fit the profile of a binary spectrum by simply superposing two single-star spectra, but the atmospheric parameters of component stars may not be correctly derived because of spectra mixing. The spectra mixing affects the profile and strength of both continuum and spectral lines. In different orbital phases, the shifted continuum has varying degrees of impact on line depth. Therefore, modelling the spectra of binary stars needs to take into account not only the intrinsic luminosity contribution of each star but also the mixing effects in different phases.

The data product of the Medium Resolution Survey of the Large sky Area Multi-Object Spectroscopic Telescope (hereafter LAMOST MRS) includes both spectra and atmospheric parameters of stars. The resolving power of LAMOST MRS is $R = 7500$, and their wavelength ranges are within 4950-5350 Å in blue arms and 6300-6800 Å in red arms, respectively.¹ The seventh data release (DR7) of LAMOST published more than 3.8 million MRS spectra including single exposure and combined spectra, and stellar parameters of 0.78 million stars with combined spectra. The MRS targeting strategies contain a series of time-domain fields (Liu et al. (2020)) and result in a large number of multiple star system spectra, including SB1 (the spectra lines are single-peaked but the radial velocities vary among different epochs), SB2 and ST (triple-lined spectra of trinary stars) spectra. Li et al. (2021) selected 3175 SB2 and 132 ST candidates using cross-correlation functions between LAMOST MRS spectra and theoretical models. Zhang et al. (2022) applied convolution neural network to develop a distinguishing model and gave a catalogue of 2198 SB2 candidates. Both Li et al. (2021) and Zhang et al. (2022) suggested that, the spectra lines of the component stars in a binary system show clear double-peaked features when their RV differences are larger than 50 km/s with LAMOST MRS resolving power of $R \sim 7500$.

It is necessary to build spectral model to derive atmospheric parameters of component stars for the LAMOST MRS SB2 spectra. The LAMOST Stellar Parameter pipeline (LASP) is the official data processing pipeline for LAMOST MRS spectra (Wu et al. (2011); Luo et al. (2015)). It was designed to derive atmospheric parameters for single stars based on the model fitting method, but was not suitable to be applied to SB2 spectra. Figure 1 shows an example of an SB2 spectrum and the “best-fit” spectrum by LASP. The upper panel is the best fitting result of the blue band, and the lower panel shows the residuals. The black line in the upper panel is the pseudo-continuum normalised observed spectrum, and the blue line is the best fitting model. The red lines stand for the LASP automatic masked points, which will not be considered in the fitting procedure. The cyan line represents the polynomial correction between the observed spectrum and the model. Mg I $\lambda 5185$, for example, is a spectral line that shows clearly a double-peaked feature, but the peaks are masked. The best-fitting model has significantly broader lines than any of the component star spectrum. The derived parameters of the SB2 spectra can not reflect the real characteristics of the component stars, so the LAMOST parameter catalogue does not contain atmospheric parameters of SB2 spectra. It’s worth developing a parameter deriving method for this kind of data.

Therefore, we mainly focus on the LAMOST MRS SB2 spectra and propose a binary star spectral modelling method to derive the atmospheric parameters for the binary stars. The method synthesises the SB2 spectral model by combining theo-

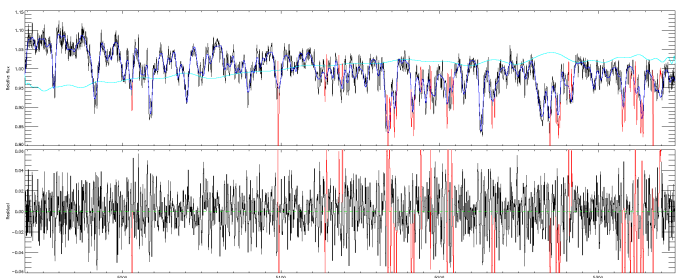


Fig. 1. LASP fitting result of an SB2 spectrum. The upper panel is the spectrum, and the lower panel is the fitting residual. The black line in the upper panel is the pseudo-continuum normalised LAMOST MRS spectrum, the blue line is the best fitting spectrum, and the cyan line represents the polynomial correction between the observed spectrum and the model. Red lines in both panels represent the masked wavelength.

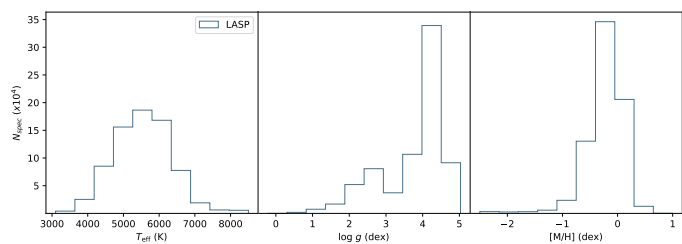


Fig. 2. Stellar parameter distribution derived by the LASP. Using the data from *LAMOST MRS Stellar Parameter Catalogue DR7 v2.0*.

retical spectra with the light curve solutions. The SB2 model is used to fit the observed binary spectra and to derive stellar parameters of the component stars. Furthermore, the method can be extended to spectroscopic data with a variety of resolutions, as long as the binary system has similar characteristics to our criteria (see details in Sect 2).

The remainder of this paper is organised as follows. Sect. 2 introduces the SB2 spectra fitting method, as well as a brief data description. Sect. 3 gives two examples of atmospheric parameters derivation. Sect. 4 is a summary section. Appendix A provides full procedures and formulae for the researchers. In Appendix B we discuss the method performance on the unresolved binary spectra observed in near-eclipsing phases.

2. Method

2.1. Data

The sources in this work are observed by both LAMOST MRS and Kepler/K2 (Batalha et al. (2010); Caldwell et al. (2010); Koch et al. (2010); Borucki et al. (2011)) or TESS (Ricker et al. (2015); Lund et al. (2017); Oelkers & Stassun (2018); Stassun et al. (2018)). And the targets must have at least three SB2 spectra in LAMOST MRS DR7 to evaluate our method’s self-consistency.

2.2. Double-lined Binary Spectral Model

A binary spectrum contains light from both component stars. The observed spectrum of each binary is affected by the distance to us, the stellar luminosity and the spectral line profiles. The line profiles are determined by the atmospheric parameters like effective temperature, the surface gravity, the metallicity, etc. Thus

¹ <http://dr7.lamost.org/v2.0/doc/mr-data-production-description>

the spectroscopic model of the binary star can be explained as follows:

$$F_{binary}(\lambda) = F_1(\lambda) + F_2(\lambda) \quad (1)$$

$$F_i(\lambda) = C \cdot L_i \cdot P_i(\lambda_i, T_{\text{eff},i}, \log g_i, [\text{M}/\text{H}]) \quad (2)$$

F_{binary} in Eq 1 is the flux of the binary. F_1 and F_2 is the flux of the component stars, separately. λ is the observed wavelength. λ_i stands for the shifted wavelength of each component in a specific orbital phase. C stands for the relationship between the luminosity and the observed flux. In the shorter wavelength range, C is considered a constant and depends on the binary's distance to us. So C has the same value for each component star. L_i represents the luminosity of each star. P_i means the spectral line profiles. In this work, we use T_{eff} , $\log g$ and $[\text{M}/\text{H}]$ to generate the theoretical continuum and line profiles simultaneously. For a binary system, T_{eff} and $\log g$ are derived for each component while the same $[\text{M}/\text{H}]$ is assigned. We omit the projected stellar rotation velocity $v_{\sin i}$ to generate the line profiles. The degeneration in surface gravity, rotational velocity, line mixing in binary spectra, and line spread function (LSF) of telescopes in line broadening can affect the accurate measurement of $\log g$. See Sect 3.2 for more details. In a binary spectrum, the profiles of one component will be affected by the line mixing and the continuum of the other. The Doppler shifts of the continuum caused by the relative motion in different orbital phases affect the profiles differently.

For spectra without absolute flux calibration, the spectra are pseudo-continuum normalised before deriving stellar parameters, and only the line features are used. After the normalisation, C in Equ 2 will be ignored for one binary system. The binary star model can be explained as:

$$f_{binary}(\lambda) = \frac{L_1}{L_1 + L_2} \cdot P_1(\lambda_1, param) + \frac{L_2}{L_1 + L_2} \cdot P_2(\lambda_2, param) \quad (3)$$

f_{binary} is the normalised binary spectrum. To obtain the luminosity contribution $\frac{L_i}{L_1+L_2}$ ($i = 1$ or 2) of each star, we choose to model the binary spectra of the detached eclipsing binaries, because the orbital parameters and luminosity contributions of the eclipsing binaries can be derived by combining the light curves and the radial velocity curves. In different phases, the component star in a detached system is not distorted significantly by the gravitation of its companion. When the stars are approximated as spheres, the projected areas of the component stars can be simply regarded as circular surfaces in the modelling.

When the light curve solution is obtained, the binary spectral model with continuum is described as:

$$F_{binary}(\lambda) = A_1 \cdot L_1 \cdot P_1(\lambda_1, T_{\text{eff},1}, \log g_1, [\text{M}/\text{H}]) + A_2 \cdot L_2 \cdot P_2(\lambda_2, r_T \cdot T_{\text{eff},1}, \log g_2, [\text{M}/\text{H}]), \quad (4)$$

and then this model spectra will be pseudo-normalised to derive stellar parameters. In this model, the luminosity contribution of each component is determined not only by its intrinsic brightness (L_i) but also by the projection area (A_i) in a specific phase. A_1 and A_2 are calculated using stellar radius R_1 and R_2 . The radii are obtained by analysing the orbital motion of the binary system. The light curves used in this work are from Kepler/K2 or TESS mission, and the radial velocity curves are reconstructed using multi-epoch LAMOST MRS SB2 spectra. We

use Wilson-Devinney binary star modelling code (WD, Wilson & Devinney (1971); Wilson (1979, 1990, 2008); Wilson & Van Hamme (2014)) through a Python UI, PyWD2015 (Güzel & Özdarcan (2020)), to derive the orbital parameters. After analysing the light curve, we get orbital period P , stellar radius R_1 and R_2 , semi-major axis SMA , orbital inclination i , eccentricity e , periastron longitude ω , mass ratio q and T_{eff} ratio r_T for the next steps. The observation epoch of the spectrum is folded into phase angle θ .

The theoretical model is computed using the SPECTRUM (Gray (2015)) base on the Kurucz ATLAS9 (Castelli & Kurucz (2003)), under the local thermodynamic equilibrium (LTE) and the plane-parallel atmosphere assumptions to generate the flux density spectra. Then we use *the Payne* (Ting et al. (2019)) to interpolate the spectra of the component stars. *The Payne* is a stellar label fitting method that consists of several ingredients. The 'interpolator' of *the Payne* applies neural networks to produce spectral model fluxes for a set of arbitrary labels. The default neural network architectures, which have two hidden layers and ten neurons for each layer, are adopted in this work. The training set of *the Payne* is the Kurucz model mentioned above and the labels are T_{eff} , $\log g$ and $[\text{M}/\text{H}]$, and the parameter range of the training set is: $4500 \leq T_{\text{eff}} \leq 8000$ K, $2.0 \leq \log g \leq 5.0$ dex, $-2.0 \leq [\text{M}/\text{H}] \leq 0.5$ dex. The ranges cover most of the LAMOST MRS observation data. Figure 2 shows the released stellar parameter distribution of LAMOST MRS DR7 v2.0. We ignore the spectral model with T_{eff} lower than 4500 K because the mixing of the molecular bands will be more complicated. After the single star spectra are interpolated by *the Payne*, we synthesise the SB2 spectra with different RVs for the component stars and the projection areas that are calculated applying the light curve solution. The pseudo-continuum normalised SB2 spectra are used to fit the observed spectra with the least square method. The SB2 model generation and the spectral fitting are iterative. In each iteration, we synthesise the SB2 model with a new set of parameters to fit the observed spectra. Both blue and red bands are generated and applied in the fitting. This is unlike the LASP, which uses only the blue band in the fitting procedure. Although the LAMOST blue band contains more information than its red band in parameter deriving (Zhang et al. (2020)), blue band is not sensitive enough to luminosity. Chen et al. (2021) suggested that the red band should also be used to derive atmospheric parameters, especially to derive $\log g$.

λ_1 and λ_2 in Equ 4 are the shifted wavelength of the component stars caused by their radial velocities RV_1 and RV_2 . The radial velocities are automatically determined in the fitting procedure. $T_{\text{eff}1}$ is the effective temperature of the hotter star and the effective temperature of the cooler star is represented by $r_T \cdot T_{\text{eff}1}$. The initial value of r_T comes from the light curve solution, and we set it to be variable in the range of ± 0.1 , although the true ratio of T_{eff} is constant. The variation of r_T actually reflects the change of relative shift of two continua in the SB2 spectra. The application of r_T can limit the spectral interpretation by the light curve characteristics and reduce the iteration times. $\log g_1$ and $\log g_2$ are the surface gravity of the two stars, respectively. Only one metallicity is derived for each spectrum.

In the non-eclipsing phases, the two component stars contribute all their fluxes to the binary spectrum. The projection area A_i is calculated according to the area of the circle. While in the eclipsing phases, eclipsing depth and surface blocking should be considered in luminosity contribution. When judging the relative distance d of the component stars, the eclipsing area can be calculated simultaneously. d can be calculated using Equ A.4 in Appendix A. Assuming that $R_1 > R_2$, the relative positions of

the component stars is obtained by comparing the values of d , $R_1 + R_2$, $R_1 - R_2$:

a. $d > (R_1 + R_2)$: The luminosity distribution in non-eclipsing phases is discussed before.

b. $d < (R_1 - R_2)$: The total eclipsing phase.

c. $(R_1 + R_2) > d > (R_1 - R_2)$: During the partially eclipsing phases, the shielded areas are approximated to the area of a portion of a circle cut by a line segment. The area calculations are described in Appendix A.

We do not consider the reflection effect and the limb darkening effect yet in this work, although they should be taken into consideration for the eclipsing phase spectra. Double-lined features in one spectrum indicate that the component stars have similar luminosity. Otherwise, the features of the less luminous star would be veiled by the other. Sometimes, the temperature difference between the primary and secondary star can be large for the situation where the cooler star has a larger radius than the hotter star. In the eclipsing phases, the reflection effect may change the magnitudes and thus the luminosity contributions. And in these phases, the limb darkening effect may reduce the luminosity contribution of the eclipsed star, which increases the difficulty of deriving its atmospheric parameters. For the LAMOST MRS spectra, when ΔRV between the two stars are smaller than $50 \text{ km} \cdot \text{s}^{-1}$, the stellar parameters derived by fitting the asymmetry of blended lines are quite different from those by the double-lined features (see Appendix B). This may be caused by the resolving power or the noise of the spectra. The parameters from the blended lines are excluded in the final results, and the neglect of the reflection effect and the limb darkening effect is ignored for LAMOST MRS SB2 spectra. But we note that for the data with higher resolution, the effects should be considered more carefully.

2.3. Continuum Influence and Method Uncertainty

In this subsection, we analyse the impact of the continuum in detail because the pseudo-normalised spectra are used in the fitting, and the line intensities of the normalised spectra will be significantly affected by the continuum. In an SB2 spectrum, the more luminous star contributes more to the continuum and will cause more impact on line intensity after normalisation. The superposition of two continua causes the relative line intensity ratio between two stars in a binary spectrum to be lower than the ratio between two single star spectra. We synthesised a series of SB2 spectra and fitted the double-peaked lines with the double-Gaussian function to see how the effect caused by luminosity and continuum varies with T_{eff} and stellar radius. Figure 3 shows the lines we chose to obtain the line intensity ratios. The upper panel of Figure 3 shows the gradient of line intensity differences of four T_{eff} gaps: 7000 – 50/100/200/500 K. The differences were calculated after each theoretical spectrum was normalised using the pseudo-continuum. We derived the gradient to find the narrow single lines that are more sensitive to effective temperature changes. If a spectral line is sensitive to T_{eff} change, the gradient shown in the upper panel of Figure 3 will be higher. The lower panel contains the related theoretical spectra in the LAMOST MRS wavelength and resolving power. Four narrow single spectral lines that are sensitive to T_{eff} changing and are less contaminated by nearby lines were selected, and they are marked by the grey dashed lines. Then we generated a series of SB2 spectra using the same model spectra as in our fitting procedures. The chosen stellar parameter ranges that are commonly contained in the LAMOST MRS DR7 data (Figure 2):

a. The metallicity is fixed to be -0.5 dex to reduce the fitting time.

b. To analyse the effect from different effective temperatures, we at first set the primary star with $T_{\text{eff}} = 7250 \text{ K}$ (T_{eff} for an F0 dwarf star) and let the secondary star have a T_{eff} various from 5350 K (T_{eff} for a G9 dwarf star) to 7250 K, with a step of 5 K. Then we choose $\log g$ equals 4.25 dex and 3.80 dex to represent the dwarf star and the sub-giant star, respectively. According to the MESA Isochrones & Stellar Tracks (MIST, Dotter (2016), Choi et al. (2016)), when the primary star is a 7250 K dwarf, it has a radius of $1.25 R_{\odot}$, and if the star is a 7250 K sub-giant, the radii is set to be $2.2 R_{\odot}$. As for the secondary star, we also set the radius to be $1.2 R_{\odot}$ and $2.2 R_{\odot}$ for dwarf stars and sub-giant stars, respectively. We fix the radius of the secondary star to reduce the affection of the stellar radius on the luminosity. The set-up is not always physical but is reasonable in most cases. Next, we generate the double-lined features with ΔRV between the two component stars equals $100 \text{ km} \cdot \text{s}^{-1}$, which is twice the ΔRV detection limitation of the LAMOST MRS SB2 spectra, to get better spectral line fitting. The SB2 spectra contain four combinations: dwarf + dwarf, sub-giant + sub-giant, dwarf + sub-giant, and sub-giant + dwarf for the primary and the secondary star, respectively. We have 1520 parameter combinations to investigate the T_{eff} various affection.

c. We also generated SB2 spectra with various radii to analyse the effect of the stellar radius. The parameter ranges are also from the MIST, although some specific combinations are not physical. To have a more prominent affection, we set the radius of the 7250 K primary star to various from $1.2 R_{\odot}$ to $3.7 R_{\odot}$ with a step of $0.02 R_{\odot}$, and the related surface gravity is between 3.5 dex and 4.3 dex. The secondary star has a T_{eff} of 6200 K (for a G0 dwarf star). The $\log g$ of a dwarf secondary star is 4.25 dex ($R = 1.2 R_{\odot}$) and of a giant secondary is 3.8 dex ($R = 2.2 R_{\odot}$), the same as in the T_{eff} various occasion. The combinations to generate binary spectra are 7250 K primary star + dwarf secondary star and 7250 K primary star + giant secondary star. We have 254 parameter combinations for the radius-changing affection.

d. In different orbital phases, the relative motions between the two component stars make the continuum of the more luminous star blue or red shift in the binary spectra. To analyse if the blue or red-shifted continuum has different effects on the line intensities, the synthesised SB2 spectra have two kinds of radial velocity settings: the primary star has a radial velocity of $-50 \text{ km} \cdot \text{s}^{-1}$ and $+50 \text{ km} \cdot \text{s}^{-1}$. ΔRV between the two components is $100 \text{ km} \cdot \text{s}^{-1}$. This procedure doubles the SB2 spectral number, so we finally have 3548 SB2 spectra for the line intensity ratio analysis, including 3040 spectra with various T_{eff} and 508 with various radii. Figure 4 shows how the line ratios change with different T_{eff} , and Figure 5 shows the changes with various radii.

e. With the same atmospheric parameters and stellar radius, but ΔRV varies from $40 \text{ km} \cdot \text{s}^{-1}$ to $120 \text{ km} \cdot \text{s}^{-1}$ randomly, we generated another 3548 SB2 spectra to evaluate the parameter fitting accuracy of our method. Figure 6 and Figure 7 show the differences between the theoretical parameters and the fitting parameters.

In Figure 4, the line ratios of different spectral lines various with T_{eff} are shown in separated panels. In each panel, different line styles represent different parameter combinations. Grey lines are the line intensity ratios between two spectra of single stars. The blue lines represent that the 7250 K components are blue-shifted in the SB2 spectra, and the orange lines mean the components are at the red-shifted phases. In the normalised sin-

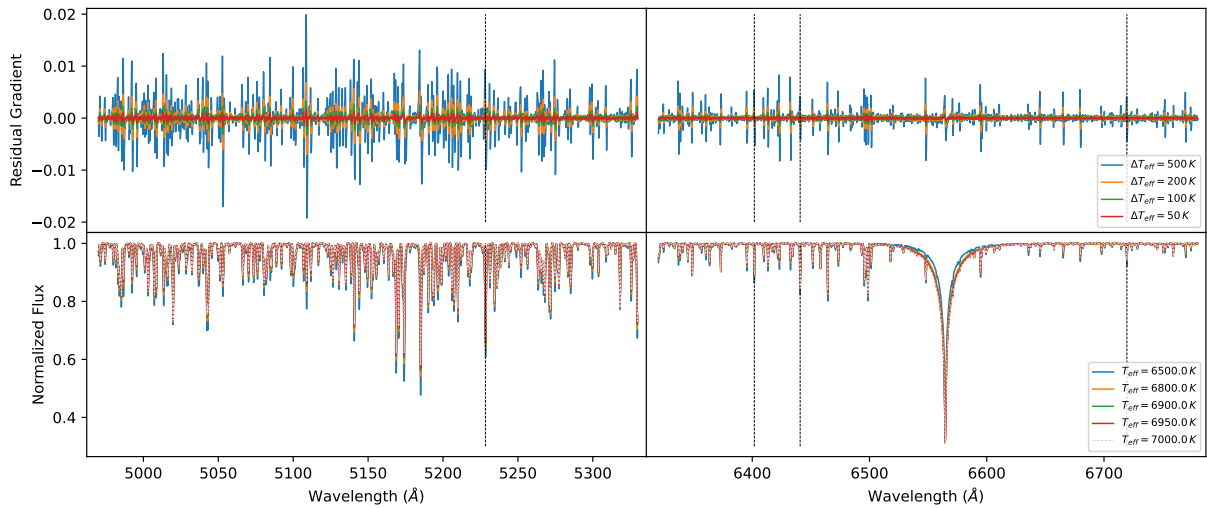


Fig. 3. The upper panel shows the gradient of line intensity differences of four T_{eff} gaps: 7000 – 50/100/200/500 K. The lower panel contains the corresponding spectra. Different colours represent spectra with different T_{eff} . The grey dashed lines indicate the spectral lines we chose to produce Figure 4 and Figure 5.

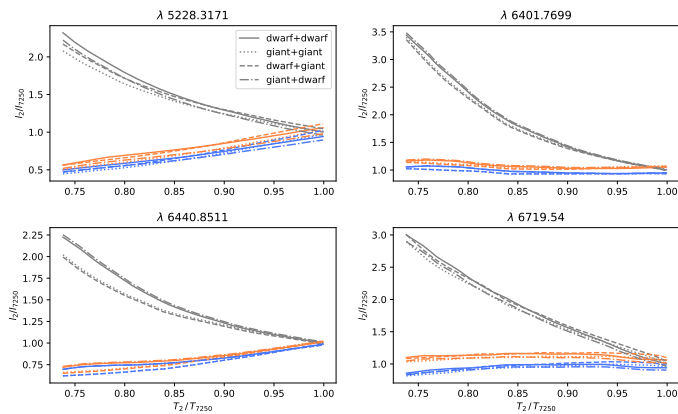


Fig. 4. The line intensity ratio between a lower T_{eff} star and a 7250 K star. The grey lines represent the ratio between two spectra of single stars, and the colourful lines are the ratio between two star components in the binary spectra. The blue lines mean that the 7250 K components are blue-shifted in SB2 spectra, and the orange lines mean that the 7250 K components are red-shifted. Different line styles stand for different parameter combinations.

gle star spectra, the relative line intensities of lower T_{eff} stars are stronger than that of the stars have $T_{\text{eff}} = 7250$ K. But in an SB2 spectrum, the superposition of two continua will reduce the relative line intensities after normalisation. The blue and the orange lines mean that the line intensities of the less luminous star are reduced more than that of the other.

Figure 5 shows how the line intensity ratios change with different radii. Line styles and colours in this figure have the same meaning as in Figure 4. The line intensity ratios don't vary a lot with stellar radius may be caused by our narrow radius selection range. The differences between the grey and the blue/orange lines also mean that the superposed continuum has more affection for the line intensities of the less luminous star.

Although the line intensities of the less luminous star are significantly reduced in the binary spectra, the blue and orange lines that have the same line style in Figure 4 and Figure 5 mean that the line intensity decrease does not vary a lot in different orbital phases. The atmospheric parameters derived in different phases (and with various ΔRV) should be consistent as long as

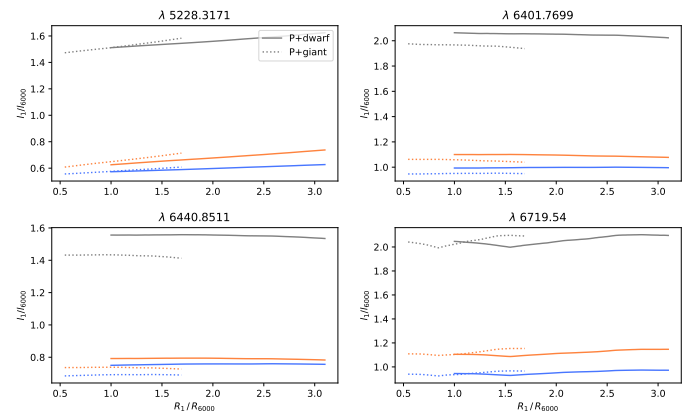


Fig. 5. The line intensity ratios change with different radii. The grey lines represent the ratio between two spectra of single stars, and the colourful lines are the ratio between two star components in the binary spectra. The blue lines mean that the 7250 K components are blue-shifted in SB2 spectra, and the orange lines mean that the 7250 K components are red-shifted. Different line styles stand for different parameter combinations.

the components can be detected. Figure 6 shows the atmospheric parameter differences of the synthetic SB2 spectra with the primary stars are in blue-shifted phases, and Figure 7 is the parameter differences when the primary stars are at red-shifted phases. Each panel contains the parameter from the fitting results of both the primary and the secondary star. The figures show that if the stellar radius and luminosity contribution are known, the fitting results will have a very low-level uncertainties for spectra without noises. So we do not consider the method uncertainties in the application on the observed SB2 spectra.

3. Examples: Atmospheric Parameters of Two SB2 Eclipsing Systems

In this section, we give two observation examples of eclipsing binaries to show the ability of our method. The examples are chosen randomly because the method is designed for binary stars that match our criteria in Sect 2. Both of the binaries have at least

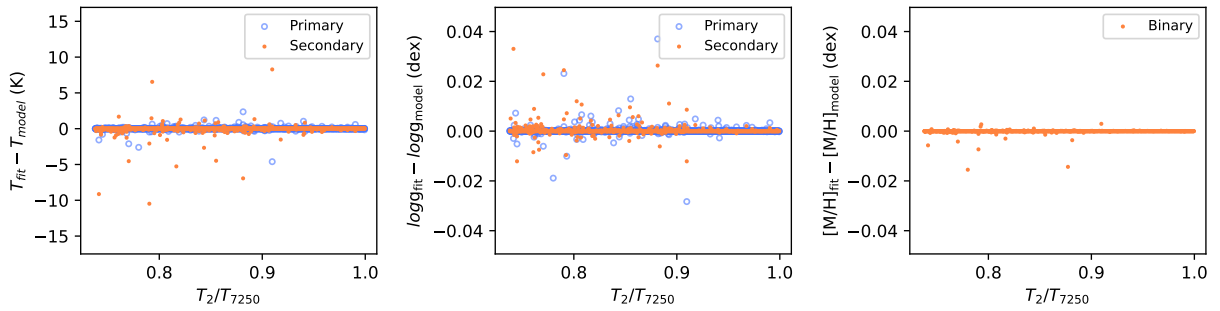


Fig. 6. Parameter differences between the measured values and the theoretical values. Blue circles in ΔT_{eff} and $\Delta \log g$ panels show the differences between the primary stars, and orange dots show the differences between the secondary stars. One metallicity is fitted for each binary system, so the $\Delta[M/H]$ panels contain only orange points. All the binaries in this figure have the primary component blue-shifted in the SB2 spectra.

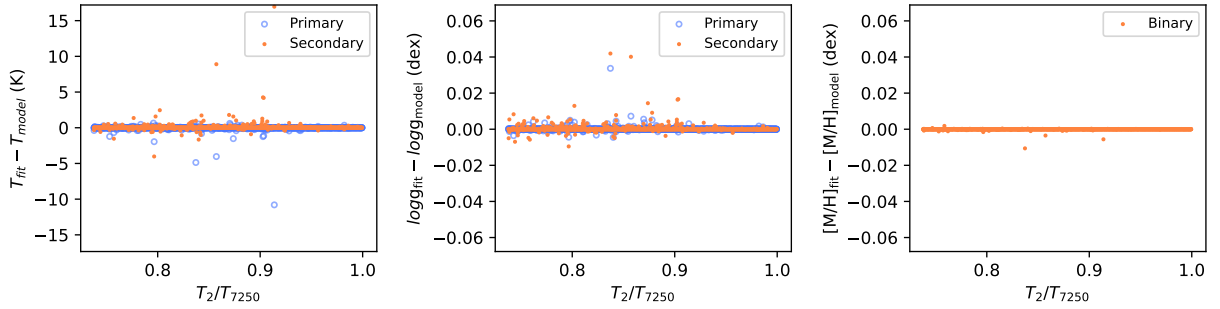


Fig. 7. Parameter differences between the measured values and the theoretical values. Colours and symbols have the same meaning as in Figure 6. All the binaries in this figure have the primary component red-shifted in the SB2 spectra.

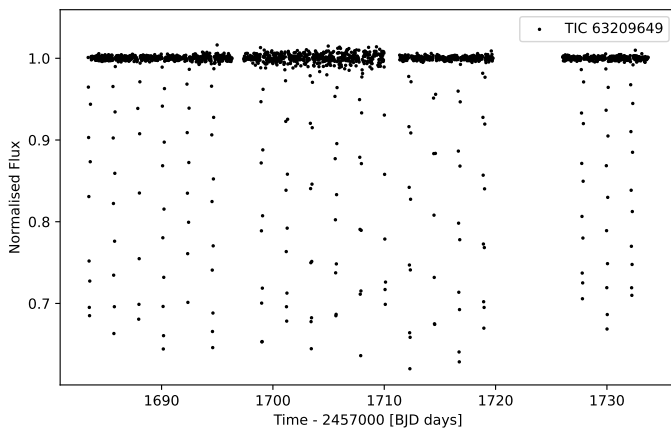


Fig. 8. Normalised TESS light curve of TIC 63209649.

three SB2 spectra in LAMOST MRS DR7 and have light curves from Kepler/K2 or TESS.

3.1. TIC 63209649

TIC 63209649 (or say KIC 8301013. TESS light curves are used in this work, so we choose the TIC number) is a detached eclipsing binary system with nine successful epochs of spectra in the LAMOST MRS DR7. Figure 8, 9 and 10 show the observation data. Figure 8 is the normalised TESS light curve. This system has a period of about 4.43 days. Figure 9 shows the normalised LAMOST MRS spectra of nine epochs. The spectra are listed in the observed time sequence, and the observation time in UTC format is shown in the upper right legend. Figure 10 shows the radial velocities of component stars in phase view. In order to reconstruct the RV curve, we firstly use *the Payne* and our binary spectral model to fit each binary spectrum. The centres of

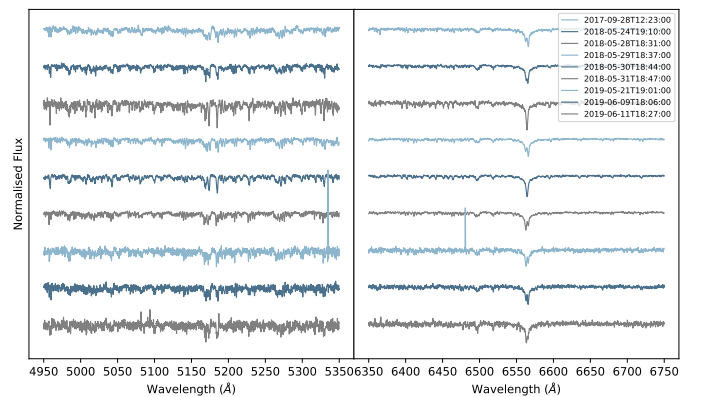


Fig. 9. Pseudo-continuum normalised LAMOST MRS multi-epoch spectra of TIC 63209649. The spectra are shown in observed time order.

strong lines can be fitted correctly to obtain the radial velocities of each star. Then we use $q = \frac{rv_1 - \gamma}{\gamma - rv_2}$ to fit q and γ . rv_1 and rv_2 are the radial velocities of the primary star and the secondary star folded in the phase order, respectively. Except for the three dots in phases 0, 0.5 and 1, other dots in Figure 10 are the measured RVs. The three dots are set manually to be γ . Finally, we reconstruct the RV curve using cosine functions. The standard deviation between the measured RVs and the best fitting lines is $5.08 \text{ km} \cdot \text{s}^{-1}$ for RV1 and $6.66 \text{ km} \cdot \text{s}^{-1}$ for RV2. Note that the fitting may be rough at the near-eclipsing phases. Combining the light curve and the radial velocity curves, we derived all the orbital parameters using the WD modelling. Figure 11 is the WD fitting result. Black dots in the upper panel represent the folded light curve, and the red line is the best fitting model. Dots in the lower panel are the residuals. The orbital parameters from the light curve solution are listed in Table 1. Combining the orbital parameters, we generated the synthetic SB2 model spectra ac-

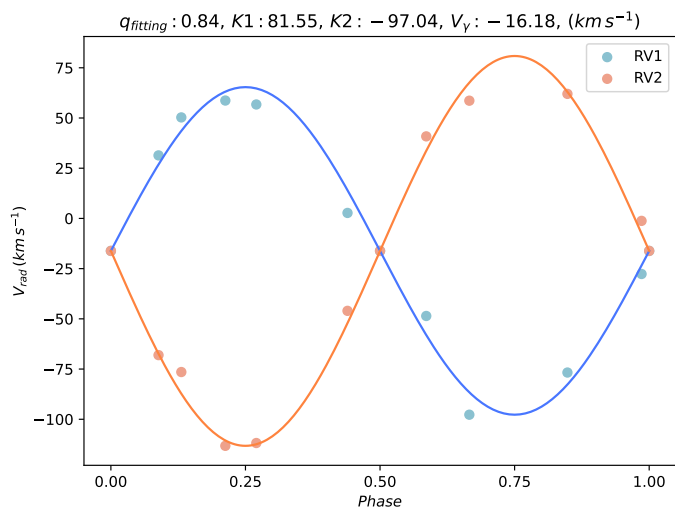


Fig. 10. The reconstructed radial velocity curves of TIC 63209649. Dots are the RVs measured by the spectra except for three dots in the phases 0, 0.5 and 1 that are set manually to be γ . Lines are the reconstructed curves. Blue represents the higher mass star and orange represents the lower mass star, respectively.

cording to equation 4, and fitted seven multi-epoch SB2 spectra of TIC 63209649. Figure 12 shows the best fitting result of one of the SB2 epochs. Black lines are the observed spectra of blue (upper panel) and red (lower panel) bands, and the red lines represent the best fitting spectra. Grey dots indicate the percentage of the residual in the observed data. Most of the residuals are below ten per cent of the observed spectra, except for residuals of some strong lines like the Mg I triplet, $\lambda 5167$, 72, 83 and the H α line. In wavebands with dense spectral lines, for example, $\lambda 5175\sim 5180$, and $\lambda 5280\sim 5285$, line mixing causes the fitting residuals to become a bit higher than the relatively line-less waveband. Two of the nine epochs were observed near eclipsing phases and did not show clear double-lined features. We present the spectral fitting results in Appendix B and give a brief discussion.

Derived atmospheric parameters of all the SB2 spectra of TIC 63209649 are listed in Table 2 in order of observation time. The orbital phases are shown in the second column. $T_{\text{eff}1}$ and $\log g_1$ are the parameters of the hotter star, and the parameters of the cooler one are $T_{\text{eff}2}$ and $\log g_2$. The metallicity of the binary system is [M/H]. The parameters of the first four epochs have a good consistency. But the results of the last three epochs are different, and they are labelled with asterisks in the first column. We checked the spectra of these three epochs and found that a poor signal-to-noise ratio might be the reason for this inconsistency. Figure 13 shows the fitting result of the last spectrum (MJD=58645) in Table 2. The noise in this spectrum is higher compared with that in Figure 12. We thus excluded this spectrum as well as the two previous noisy spectra before parameter averaging. Atmospheric parameters in the last row of Table 2 are the mean values of the adopted epoch results. We take the standard deviations as the measurement errors and list them in the parentheses. The errors are at the same level as the errors of LASP parameters of the single stars (Chen et al. (2021)).

3.2. EPIC 247529791

The K2 target EPIC 247529791 is also a detached eclipsing binary with a nearly circular orbit. Figure 14 is the normalised

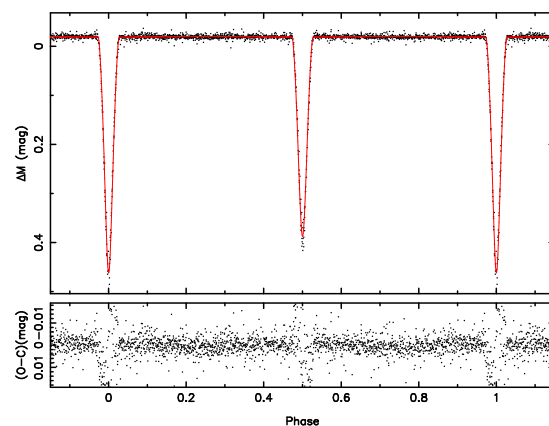


Fig. 11. WD fitting result of the TIC 63209649 light curve. Black dots in the upper panel are the observed data and the red line is the best fitting model. The lower panel shows the fitting residuals.

Table 1. Orbital parameters of TIC 63209649.

| Parameter | Primary | System | Secondary |
|------------------------|---------|---------------------|-----------|
| $t_{\text{conj}} (d)$ | | 2458685.7373 | |
| $P (d)$ | | 4.4275 | |
| $\gamma (km s^{-1})$ | | -16.1754 | |
| q | | 0.8403 | |
| $a \sin i (R_{\odot})$ | | 16.11 ± 0.053 | |
| $i (^{\circ})$ | | 87.44 ± 0.03 | |
| e | | 0.0299 ± 0.0177 | |
| $\omega (^{\circ})$ | | 90.25 ± 0.22 | |
| r_T | | 0.9700 | |
| $R (R_{\odot})$ | 1.5093 | | 1.2297 |
| $M (M_{\odot})$ | 1.4305 | | 1.2016 |
| $\log g (\text{dex})$ | 4.24 | | 4.34 |

K2 light curve. The orbital period is 3.94 days. Figure 15 shows LAMOST MRS spectra of five epochs in time sequence. The latest spectrum has a bad signal-to-noise ratio, so we excluded it in the fitting procedures. Figure 16 shows the reconstructed radial velocity curves. The curves are fitted by the same procedures as in Sect 3.1 and the symbols and lines have the same meaning as in Figure 10. The standard deviation between the measured RVs and the best fitting lines are $0.33 \text{ km} \cdot \text{s}^{-1}$ for RV1 and $0.98 \text{ km} \cdot \text{s}^{-1}$ for RV2. The orbital parameters are also derived using WD and Figure 17 is the best fitting model. The orbital parameters are listed in Table 3. The model synthesising and spectra fitting is the same as above. Three of the four higher S/N spectra show double-lined features and are used to derive stellar parameters. Figure 18 is an example of best-fitting results. In most of the wavelengths, the residuals have the same level as in Figure 12. The fitting result of the unresolved spectrum is also discussed in Appendix B.

Table 4 shows the atmospheric parameters of SB2 spectra fitting. T_{eff} and [M/H] derived from different phases have good consistency, but $\log g$ of the secondary star can not be derived robustly. Two reasons may explain this phenomenon. First, the lower S/N influences the fitting result a lot. Second, the most prominent line features in the LAMOST MRS spectra are the Mg I triplet, $\lambda 5167$, 72, 83 lines in the blue band, and the H α line in the red band. The Mg I triplet lines are not sensitive enough to luminosity (Guinan & Smith (1984a)), and their line profiles are easily influenced when ΔRV between component stars get larger.

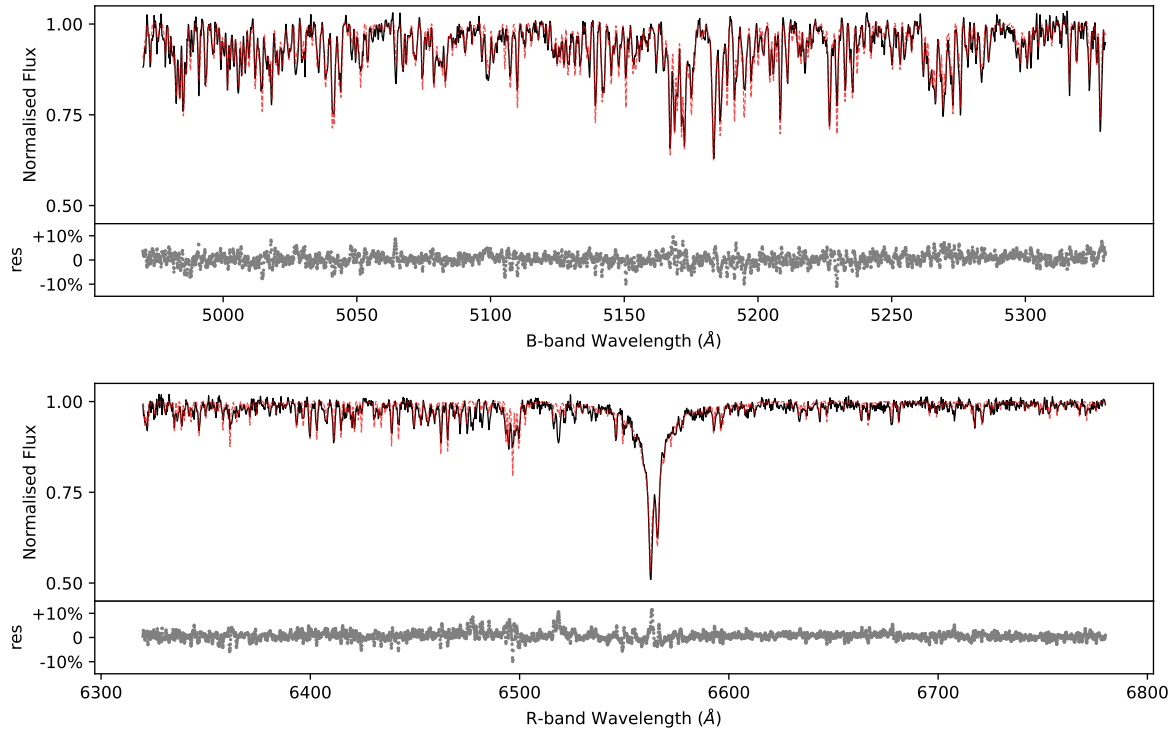


Fig. 12. A best-fitting example of the TIC 63209649 SB2 spectrum. Black lines are the LAMOST MRS spectra and red lines are the best fitting synthetic SB2 model. Grey dots represent the fitting residuals.

Table 2. Atmospheric parameters of the TIC 63209649 component stars. Lines with asterisks are excluded before deriving the final parameters because of the low signal-to-noise ratios.

| MJD | Phase | $T_{\text{eff}1}$ (K) | $\log g_1$ (dex) | $T_{\text{eff}2}$ (K) | $\log g_2$ (dex) | [M/H] (dex) |
|-----------|--------|-----------------------|------------------|-----------------------|------------------|-------------|
| 58024 | 0.2702 | 6724.98 | 4.18 | 5946.48 | 3.78 | -0.34 |
| 58262 | 0.0885 | 6596.99 | 4.08 | 5962.63 | 3.83 | -0.07 |
| 58267 | 0.2126 | 6614.74 | 3.94 | 5880.60 | 3.73 | -0.37 |
| 58269 | 0.6659 | 6636.17 | 4.30 | 5879.86 | 3.79 | -0.14 |
| 58624 * | 0.8481 | 6386.38 | 3.56 | 5966.20 | 4.45 | 0.10 |
| 58643 * | 0.1308 | 6232.98 | 3.69 | 5678.84 | 4.25 | -0.28 |
| 58645 * | 0.5858 | 6140.11 | 3.58 | 5817.86 | 3.56 | -0.25 |
| Mean(Std) | - | 6643.22(49.20) | 4.13(0.13) | 5917.39(37.60) | 3.78(0.04) | -0.23(0.13) |

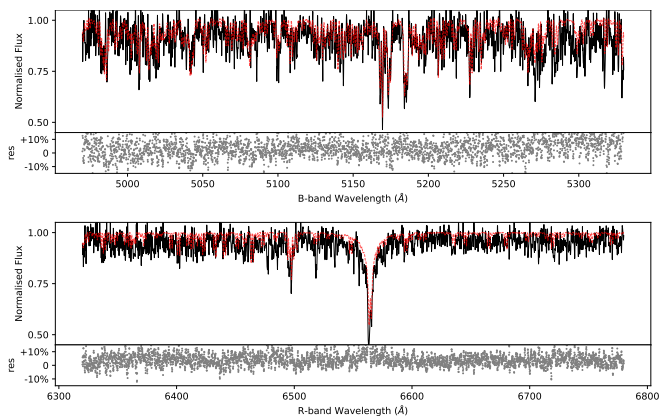


Fig. 13. A fitting example of a TIC 63209649 spectrum with a low signal-to-noise ratio. Colours and symbols have the same meaning as in Figure 12.

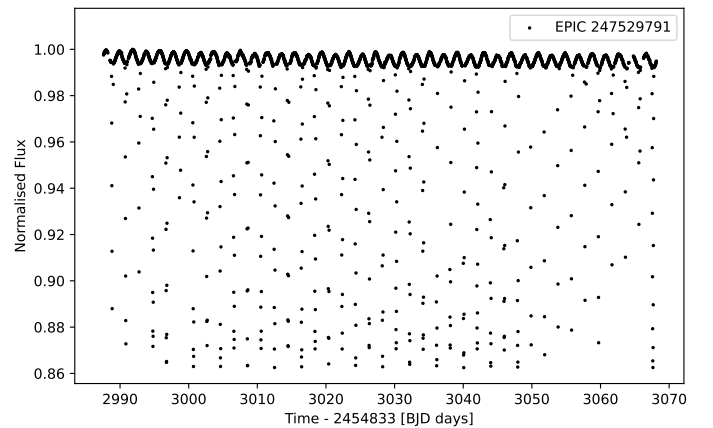


Fig. 14. Normalised K2 light curve of EPIC 247529791.

Although combining the red band in the fitting procedure can improve the $\log g$ derivation (Chen et al. (2021), Figure 11~12),

the wings of the $H\alpha$ line are also significantly affected by the mixing of two components.

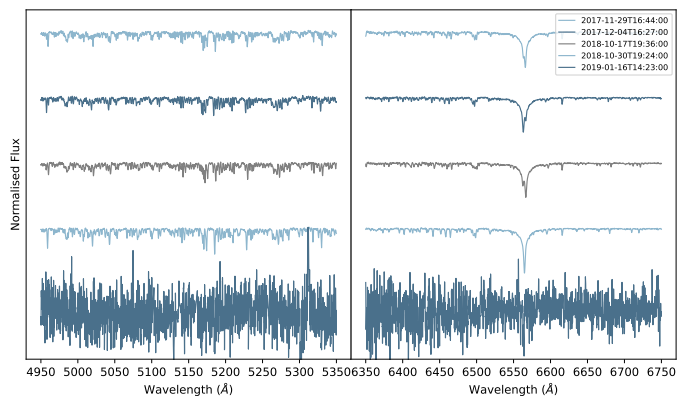


Fig. 15. Pseudo-continuum normalised LAMOST MRS multi-epoch spectra of EPIC 247529791. The spectra are shown in observed time order.

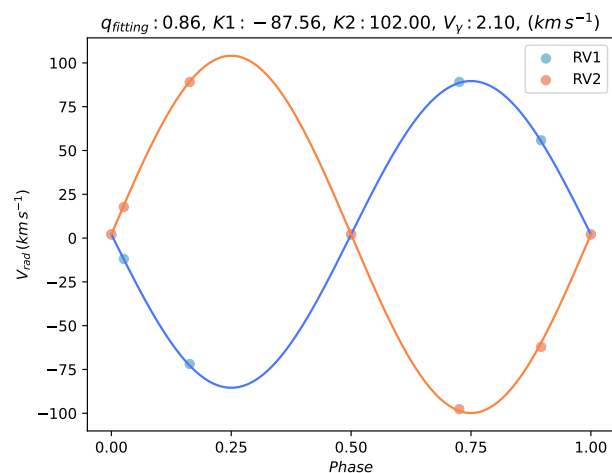


Fig. 16. The reconstructed radial velocity curves of EPIC 247529791. Dots are the RVs measured by the spectra except for three dots in the phases 0, 0.5 and 1 that are set manually to be γ . Lines are the reconstructed curves. Blue represent the higher mass star and orange represent the lower mass star, respectively.

The atmospheric parameters of component stars in the EPIC 247529791 system were also derived by Traven et al. (2020) (hereafter Traven2020). The GALAH DR2 specID of this binary is 17013100180129. In that work, they used photometry data to reconstruct the SED of the binaries and then applied the Bayesian inference and a Monte Carlo Markov chain sampler (Gregory (2005); Hogg et al. (2010); Foreman-Mackey et al. (2013); Sharma (2017)) to derive atmospheric parameters. The Traven2020 parameters are listed in Table 5. Metallicities of the system derived in our work and by Traven2020 have a good consistency. For the warmer component star, our method gets higher T_{eff} than Traven2020, while for the cooler star, our T_{eff} is lower than the result of Traven2020. The $\log g$ of the warmer star obtained by the two methods are similar. The $\log g$ of the cooler star in our results is lower than in the Traven2020 results. Furthermore, both $\log g$ of the cooler star derived in the two works is lower than that in the light curve solution in Table 3.

Different resolving power and fitting methods may cause the inconsistency of the derived parameters. (1) The LAMOST MRS with $R \sim 7500$ has a lower resolution than GALAH ($R \sim 28000$). Line mixing caused by the Doppler shift of the component stars makes recognising features of the fainter star more difficult, and

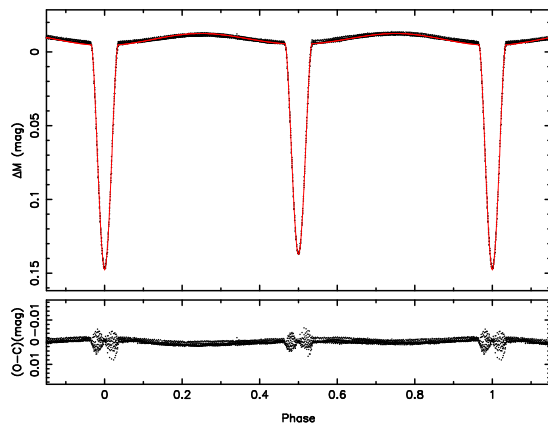


Fig. 17. WD fitting result of the EPIC 247529791 light curve. Black dots in the upper panel are the observed data and the red line is the best fitting model. The lower panel shows the fitting residuals.

Table 3. Orbital parameters of EPIC 247529791.

| Parameter | Primary | System | Secondary |
|------------------------|---------|---------------------|-----------|
| $t_{\text{conj}} (d)$ | | 2457821.8943 | |
| $P (d)$ | | 3.9365 | |
| $\gamma (km s^{-1})$ | | 2.1000 | |
| q | | 0.8585 | |
| $a \sin i (R_{\odot})$ | | 14.60 ± 0.023 | |
| $i (^{\circ})$ | | 80.803 ± 0.006 | |
| e | | 0.0072 ± 0.0015 | |
| $\omega (^{\circ})$ | | 84.6 ± 2.9 | |
| r_T | | 0.9709 | |
| $R (R_{\odot})$ | 2.3715 | | 1.5946 |
| $M (M_{\odot})$ | 1.5576 | | 1.3395 |
| $\log g (\text{dex})$ | 3.88 | | 4.16 |

makes deriving atmospheric parameters imprecisely in the lower resolution spectra. (2) We use the Kurucz theoretical spectra as our fitting model, while Traven2020 adopted a series of observed spectra to be the fitting template, same as the GALAH official pipeline (Kos et al. (2017)). (3) The binary spectra models are produced in different ways. In our work, we synthesise the binary spectra with the light curve-derived radii and the phase-based projection areas. The luminosity contribution depends on the real size and T_{eff} ratio of the component stars. Traven2020 generated the synthetic SED of two single stars using the Kurucz ATLAS9 models and produced the SED of the binary system taking the component star radii as the independent variables. The generated binary SED and the radii were restricted by the apparent magnitudes from AAVSO Photometric All-Sky Survey – APASS (Henden et al. (2016)), Gaia DR2 (Evans et al. (2018)), Two Micron All Sky Survey – 2MASS (Skrutskie et al. (2006)), and Wide-field Infrared Survey Explorer – WISE (Wright et al. (2010)).

Except for the difference between the two methods, we suggest other two factors that may cause the inconsistency. The two factors may also be the disadvantages of deriving atmospheric parameters using the SB2 spectra.

First, the effect of mixing and continuum contamination on the line depth influence T_{eff} measurement. Theoretically, the prime criteria to derive the effective temperature for a main-sequence F-type star are the strength and profiles of the hydrogen lines (Gray & Corbally (2009)). But the LAMOST MRS wave-

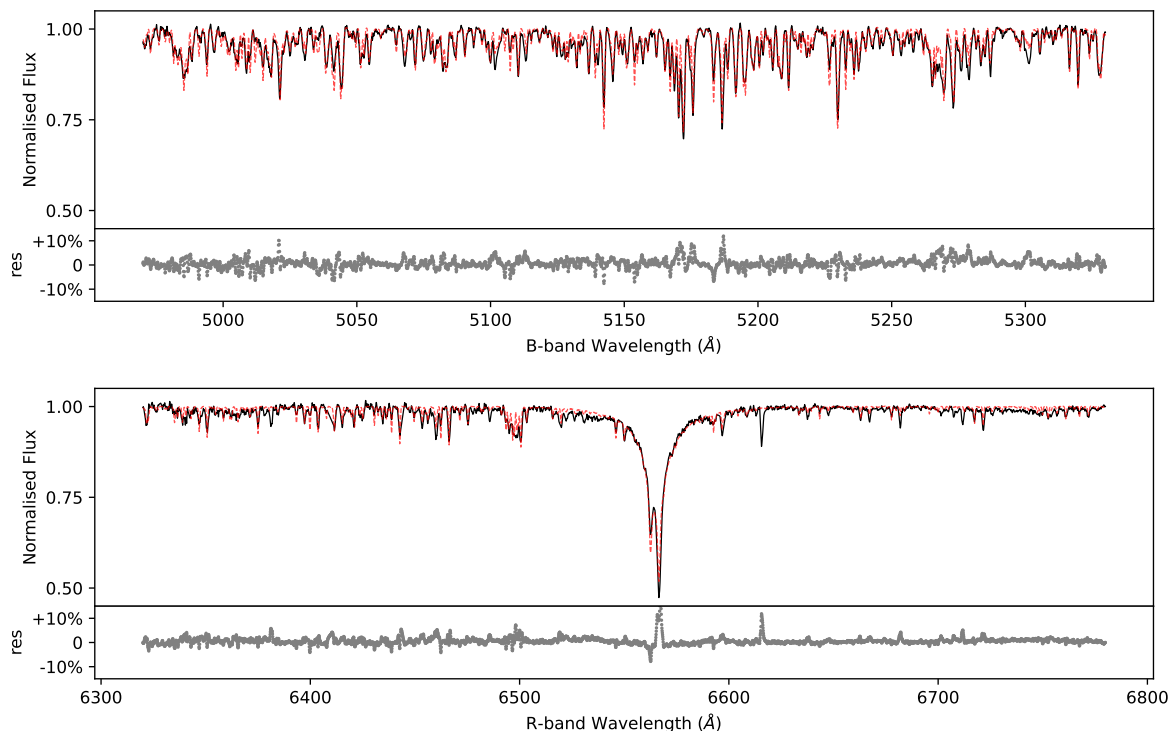


Fig. 18. A best-fitting example of the EPIC 247529791 SB2 spectrum. Black lines are the LAMOST MRS spectra and red lines are the best fitting synthetic SB2 model. Grey dots represent the fitting residuals.

Table 4. Atmospheric parameters of the EPIC 247529791 component stars.

| MJD | Phase | $T_{\text{eff}1}$ (K) | $\log g_1$ (dex) | $T_{\text{eff}2}$ (K) | $\log g_2$ (dex) | [M/H] (dex) |
|------------|--------|-----------------------|------------------|-----------------------|------------------|--------------|
| 58086 | 0.8963 | 6949.89 | 3.58 | 6180.68 | 3.73 | -0.46 |
| 58091 | 0.1634 | 6969.50 | 3.47 | 6166.86 | 3.00 | -0.43 |
| 58408 | 0.7257 | 6989.81 | 3.62 | 6092.99 | 3.44 | -0.48 |
| Mean (Std) | - | 6969.73 (16.30) | 3.56 (0.06) | 6146.84 (38.50) | 3.39 (0.30) | -0.46 (0.02) |

Table 5. Atmospheric parameters of the EPIC 247529791 derived by Traven2020.

| Parameter | Value |
|-----------------------|---------|
| R_1 (R_{\odot}) | 1.65 |
| $T_{\text{eff}1}$ (K) | 6729.99 |
| $\log g_1$ (dex) | 3.67 |
| R_2 (R_{\odot}) | 2.77 |
| $T_{\text{eff}2}$ (K) | 6431.46 |
| $\log g_2$ (dex) | 3.80 |
| [M/H] (dex) | -0.42 |

band contains only the $H\alpha$ line. Due to its depth and broad width, the $H\alpha$ line is easily influenced by the mixing of two spectra. In this case, the metal lines become the main features to derive T_{eff} . But metal lines are shallower than the $H\alpha$ lines; the absolute strength is more easily affected by the continuum. And the relative line intensity ratio is constrained by the luminosity contribution. When fitting the SB2 spectrum, the more luminous star component occupies more weight in fitting the best model. This makes the measured T_{eff} of the hotter star higher than the real value. The two reasons say the relative line intensity change and the higher measured T_{eff} of the hotter star cause the T_{eff} ratio to get smaller in the fitting iteration, which makes the T_{eff} measure-

ment of the cooler star to be lower. Absolute flux calibration may help to reduce continuum contamination.

Second, the surface gravity of the component stars by fitting the SB2 spectra are underestimated. Since the most prominent spectral lines in the LAMOST MRS waveband are the MgI triplet $\lambda\lambda$ 5167, 72, 83 and the $H\alpha$, the surface gravity of most of the A- to G-type MS stars can not be derived precisely (Chen et al. (2021)). Wings of the hydrogen lines are luminosity sensitive for early A-type stars, and the MgI triplet is for late G- to mid-K-type stars (Guinan & Smith (1984b)). Furthermore, the micro-turbulent velocity plays an important role in determining surface gravity for the F-, G- and even K-type stars. For the mid-F-type dwarfs, a micro-turbulent velocity of about two $\text{km} \cdot \text{s}^{-1}$ affects the luminosity criteria (Gray et al. (2001)). The spectral lines in a single star spectrum are broader and stronger due to the micro-turbulence. In an SB2 spectrum, Doppler shift and line mixing cause the double-peaked lines to be broader and stronger than the lines in a single-star spectrum. Under the joint influence of the micro-turbulence and the line mixing, deriving $\log g$ directly from the SB2 spectra underestimates the measured results. Although Traven2020 accounted for the micro-turbulent velocity, the spectral line mixing still makes sense, resulting in the $\log g$ measurements that are smaller than the light curve solution.

4. Summary

We provide a method to model the binary star spectra with double-lined features. The antecedent information of a detached eclipsing binary system is derived by solving the light curves and radial velocity curves. We synthesise the SB2 model spectra by superposing single star spectra according to the luminosity contribution of the component stars. The synthetic spectra are then used to fit the observation spectra by the least square method and derive atmospheric parameters of the component stars. The method provides radial velocities, effective temperatures and surface gravity of each star, and metallicity for the binary system. We generate model spectra for different phases according to the change of the relative position of the component stars. The atmospheric parameters derived from the multi-epoch SB2 spectra have similar values, which indicates the robustness of our method.

Our method gives the way to calculate effective projection areas of component stars in both eclipsing and non-eclipsing phases. But in the fitting experiments shown in Sect 3, we find that the LAMOST MRS SB2 spectra were observed mostly in the non-eclipsing phases. With the resolution of 7500, LAMOST MRS can not resolve double-lined features in nearly eclipsing phases. So the LAMOST MRS SB2 spectra contain fluxes from the whole system of stars.

This method can also be applied to partial eclipsing spectra as long as the resolution is high enough to resolve binary features. Besides, with the increase of resolution, the influence of the limb darkening effect, the reflection between two stars and the microturbulence on the spectral line begins to appear and should be considered in determining atmospheric parameters.

Acknowledgements. The authors thank the reviewer for useful comments to the manuscript. This work is supported by National Science Foundation of China (Nos U1931209, 11970360, 12003050, 12090044, 12103068) and National Key R&D Program of China (Nos. 2019YFA0405102, 2019YFA0405502). Guoshoujing Telescope (the Large Sky Area Multi-Object Fibre Spectroscopic Telescope, LAMOST) is a National Major Scientific Project built by the Chinese Academy of Sciences. Funding for the project has been provided by the National Development and Reform Commission. LAMOST is operated and managed by the National Astronomical Observatories, Chinese Academy of Sciences. This paper includes data collected by the Kepler mission and obtained from the MAST data archive at the Space Telescope Science Institute (STScI). Funding for the Kepler mission is provided by the NASA Science Mission Directorate. STScI is operated by the Association of Universities for Research in Astronomy, Inc., under NASA contract NAS 5–26555. This paper includes data collected with the TESS mission, obtained from the MAST data archive at the Space Telescope Science Institute (STScI). Funding for the TESS mission is provided by the NASA Explorer Program. STScI is operated by the Association of Universities for Research in Astronomy, Inc., under NASA contract NAS 5–26555.

References

Batalha, N. M., Borucki, W. J., Koch, D. G., et al. 2010, *ApJ*, 713, L109
 Borucki, W. J., Koch, D. G., Basri, G., et al. 2011, *ApJ*, 736, 19
 Caldwell, D. A., Kolodziejczak, J. J., Van Cleve, J. E., et al. 2010, *ApJ*, 713, L92
 Castelli, F. & Kurucz, R. L. 2003, in *Modelling of Stellar Atmospheres*, ed. N. Piskunov, W. W. Weiss, & D. F. Gray, Vol. 210, A20
 Chen, H.-L., Woods, T. E., Yungelson, L. R., Gilfanov, M., & Han, Z. 2015, *MNRAS*, 453, 3024
 Chen, X.-L., Luo, A. L., Chen, J.-J., et al. 2021, *PASP*, 133, 044502
 Choi, J., Dotter, A., Conroy, C., et al. 2016, *ApJ*, 823, 102
 Dotter, A. 2016, *ApJS*, 222, 8
 Duchêne, G. & Kraus, A. 2013, *ARA&A*, 51, 269
 El-Badry, K., Ting, Y.-S., Rix, H.-W., et al. 2018, *MNRAS*, 476, 528
 Evans, D. W., Riello, M., De Angeli, F., et al. 2018, *A&A*, 616, A4
 Foreman-Mackey, D., Hogg, D. W., Lang, D., & Goodman, J. 2013, *PASP*, 125, 306
 Göteborg, Y., de Mink, S. E., McQuinn, M., et al. 2020, *A&A*, 634, A134
 Gray, R. 2015
 Gray, R. & Corbally, C. 2009, *Stellar Spectral Classification*

Gray, R. O., Graham, P. W., & Hoyt, S. R. 2001, *AJ*, 121, 2159
 Gregory, P. 2005, *The how-to of Bayesian inference* (Cambridge University Press), 41–71
 Guinan, E. F. & Smith, G. H. 1984a, *PASP*, 96, 354
 Guinan, E. F. & Smith, G. H. 1984b, *PASP*, 96, 354
 Güzel, O. & Özdarcan, O. 2020, *Contributions of the Astronomical Observatory Skalnaté Pleso*, 50, 535
 Han, Z. 1998, *MNRAS*, 296, 1019
 Han, Z., Podsiadlowski, P., & Lynas-Gray, A. E. 2007, *MNRAS*, 380, 1098
 Han, Z.-W., Ge, H.-W., Chen, X.-F., & Chen, H.-L. 2020, *Research in Astronomy and Astrophysics*, 20, 161
 Henden, A. A., Templeton, M., Terrell, D., et al. 2016, *VizieR Online Data Catalog*, II/336
 Hogg, D. W., Bovy, J., & Lang, D. 2010, *arXiv e-prints*, arXiv:1008.4686
 Hoyle, F. & Fowler, W. A. 1960, *ApJ*, 132, 565
 Iben, I. J. & Tutukov, A. V. 1984, *ApJS*, 54, 335
 Izzard, R. G., Glebbeek, E., Stancliffe, R. J., & Pols, O. R. 2009, *A&A*, 508, 1359
 Koch, D. G., Borucki, W. J., Basri, G., et al. 2010, *ApJ*, 713, L79
 Kos, J., Lin, J., Zwitter, T., et al. 2017, *MNRAS*, 464, 1259
 Li, C.-q., Shi, J.-r., Yan, H.-l., et al. 2021, *ApJS*, 256, 31
 Liu, C., Fu, J., Shi, J., et al. 2020, *arXiv e-prints*, arXiv:2005.07210
 Lund, M. N., Handberg, R., Kjeldsen, H., Chaplin, W. J., & Christensen-Dalsgaard, J. 2017, in *European Physical Journal Web of Conferences*, Vol. 160, *European Physical Journal Web of Conferences*, 01005
 Luo, A. L., Zhao, Y.-H., Zhao, G., et al. 2015, *Research in Astronomy and Astrophysics*, 15, 1095
 Oelkers, R. J. & Stassun, K. G. 2018, *AJ*, 156, 132
 Raghavan, D., McAlister, H. A., Henry, T. J., et al. 2010, *ApJS*, 190, 1
 Ricker, G. R., Winn, J. N., Vanderspek, R., et al. 2015, *Journal of Astronomical Telescopes, Instruments, and Systems*, 1, 014003
 Secunda, A., Cen, R., Kimm, T., Göteborg, Y., & de Mink, S. E. 2020, *ApJ*, 901, 72
 Sharma, S. 2017, *ARA&A*, 55, 213
 Skrutskie, M. F., Cutri, R. M., Stiening, R., et al. 2006, *AJ*, 131, 1163
 Stassun, K. G., Oelkers, R. J., Pepper, J., et al. 2018, *AJ*, 156, 102
 Ting, Y.-S., Conroy, C., Rix, H.-W., & Cargile, P. 2019, *ApJ*, 879, 69
 Travençolo, G., Feltzing, S., Merle, T., et al. 2020, *A&A*, 638, A145
 Webbink, R. F. 1984, *ApJ*, 277, 355
 Whelan, J. & Iben, I. 1973, *ApJ*, 186, 1007
 Wilson, R. E. 1979, *ApJ*, 234, 1054
 Wilson, R. E. 1990, *ApJ*, 356, 613
 Wilson, R. E. 2008, *ApJ*, 672, 575
 Wilson, R. E. & Devinney, E. J. 1971, *ApJ*, 166, 605
 Wilson, R. E. & Van Hamme, W. 2014, *ApJ*, 780, 151
 Wright, E. L., Eisenhardt, P. R. M., Mainzer, A. K., et al. 2010, *AJ*, 140, 1868
 Wu, Y., Luo, A. L., Li, H.-N., et al. 2011, *Research in Astronomy and Astrophysics*, 11, 924
 Zhang, B., Jing, Y.-J., Yang, F., et al. 2022, *ApJS*, 258, 26
 Zhang, B., Liu, C., Li, C.-Q., et al. 2020, *Research in Astronomy and Astrophysics*, 20, 051

Appendix A: Projection Areas Calculation

1. Basic Assumptions: Spherical component stars.
2. Initial data:
 - 2.1 Fit RV curves and mass ratio q using spectra radial velocities.
 - 2.2 Period(P), eccentricity(e), inclination(i), argument of periastron (ω), time of periastron passage t_{per} , semi major axis(SMA), radii of component stars (suppose $R_1 > R_2$).
3. Projection areas:

Figure A.1 is a schematic of the projection areas during shallow partial eclipse. The specific calculation is as follows:

 - 3.1 At the observation time t of an SB2 spectrum, the mean anomaly M , the eccentric anomaly E and the true anomaly ν of the binary system are calculated as following:

$$M = 2\pi \frac{t - t_{per}}{P}, \quad (\text{A.1})$$

$$E - e \sin E = M, \quad (\text{A.2})$$

$$\tan \frac{E}{2} = \sqrt{\frac{1-e}{1+e}} \tan \frac{\nu}{2}. \quad (\text{A.3})$$

- 3.2 Projection distance d between the component stars onto the plane-of-sky:

$$d = SMA \frac{1 - e^2}{1 + e \cos \nu} [1 - \sin^2(\omega + \nu) \sin^2 i]^{1/2}. \quad (\text{A.4})$$

- 3.3 Projection areas during different phases:

- 3.3.1 No eclipse ($d > R_1 + R_2$):

$$\begin{aligned} A_{1ini} &= \pi \cdot R_1^2, \\ A_{2ini} &= \pi \cdot R_2^2. \end{aligned} \quad (\text{A.5})$$

- 3.3.2 Total and annular eclipse ($d < R_1 - R_2$): when the larger one is in front (total eclipse):

$$\begin{aligned} A_1 &= A_{1ini}, \\ A_2 &= 0. \end{aligned} \quad (\text{A.6})$$

When the smaller one is in front (annular eclipse):

$$\begin{aligned} A_1 &= A_{1ini} - A_{2ini}, \\ A_2 &= A_{2ini}. \end{aligned} \quad (\text{A.7})$$

- 3.3.3 Partial eclipse:

- a. Shallow partial eclipse ($d > \sqrt{R_1^2 - R_2^2}$):

- larger one in front:

$$\begin{aligned} A_1 &= A_{1ini}, \\ A_2 &= A_{2ini} - \Delta A_1 - \Delta A_2. \end{aligned} \quad (\text{A.8})$$

- smaller one in front:

$$\begin{aligned} A_1 &= A_{1ini} - \Delta A_1 - \Delta A_2, \\ A_2 &= A_{2ini}. \end{aligned} \quad (\text{A.9})$$

- b. Deep partial eclipse ($\sqrt{R_1^2 - R_2^2} > d > R_1 - R_2$):

- larger one in front:

$$\begin{aligned} A_1 &= A_{1ini}, \\ A_2 &= \Delta A_2 - \Delta A_1. \end{aligned} \quad (\text{A.10})$$

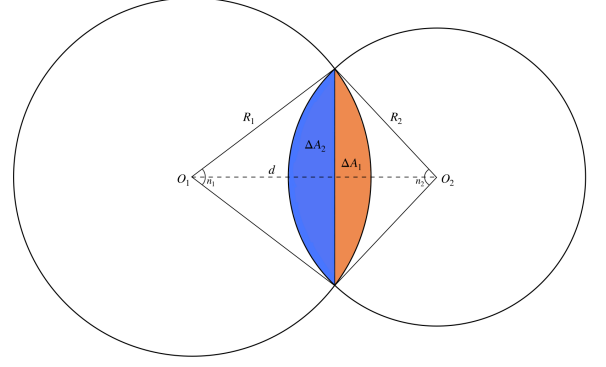


Fig. A.1. Schematic diagram of the projection areas. O_1 and O_2 represent the projected centres of the stellar discs, and d is the distance between them. R_1 and R_2 stand for the radii of the component stars. The areas ΔA_1 and ΔA_2 vary in different orbital phases. See step 3 in Appendix A for their calculation.

- smaller one in front:

$$\begin{aligned} A_1 &= A_{1ini} - A_{2ini} - \Delta A_1 + \Delta A_2, \\ A_2 &= A_{2ini}. \end{aligned} \quad (\text{A.11})$$

ΔA_1 and ΔA_2 are approximated to the area of a portion of a circle cut by a line segment.

$$\Delta A_i = \frac{1}{2} R_i^2 (n_i - \sin(n_i)), \quad i = 1 \text{ or } 2. \quad (\text{A.12})$$

n_1 and n_2 (in radian) in the above equations represent the central angle corresponding to the two circles meeting chord on each projection of the stellar surface. They can be calculated by:

$$\begin{aligned} n_1 &= 2 \arccos\left(\frac{d^2 + R_1^2 - R_2^2}{2dR_1}\right), \\ n_2 &= 2 \arccos\left(\frac{d^2 - R_1^2 + R_2^2}{2dR_2}\right). \end{aligned} \quad (\text{A.13})$$

Appendix B: Fitting Spectra from Near-Eclipsing Phases

At the near-eclipsing phases, although the double-line features can not be recognised in the LAMOST MRS resolution, the asymmetry of lines is caused when $\Delta RV < 50 \text{ km} \cdot \text{s}^{-1}$. We present the spectral fitting results of two near-eclipsing spectra. Figure B.1 shows the best fitting model of a TIC 63209649 spectrum. The black lines are the LAMOST MRS spectra, the red dashed lines are the best fitting model, and the grey dotted lines represent the residuals. Although the spectrum can be fitted by a synthetic binary spectrum with the help of the orbital results, the atmospheric parameters are quite different from the results of the SB2 spectra. The best fitting parameters of Figure B.1 are: $T_{\text{eff}1} = 6263.63 \text{ K}$, $\log g_1 = 3.75 \text{ dex}$ for the primary star, $T_{\text{eff}2} = 6220.43 \text{ K}$, $\log g_2 = 4.44 \text{ dex}$ for the secondary star, and $[M/H] = -0.48 \text{ dex}$ for the binary system. But the mean parameters of the SB2 spectral fitting are: $T_{\text{eff}1} = 6643.22 \pm 49.20 \text{ K}$, $\log g_1 = 4.13 \pm 0.13 \text{ dex}$ for the primary star, $T_{\text{eff}2} = 5917.39 \pm 37.60 \text{ K}$, $\log g_2 = 3.78 \pm 0.04 \text{ dex}$ for the secondary star, and $[M/H] = -0.23 \pm 0.13 \text{ dex}$ for the binary system (Table 2). In Sect. 2.3, we find the atmospheric parameters derived in different phases should not vary a lot if the contributions of the component stars are detected correctly. Therefore,

the fitting results in the figure are likely to be inconsistent with the real situation. We suggest that the real signal-to-noise ratio (S/N) of the near-eclipsing spectrum is not high enough to recognise the line asymmetry correctly, despite the announced S/N of this spectrum being 60.42 for the blue band and 94.05 for the red band in the LAMOST MRS catalogue.

Figure B.2 is the near-eclipsing phase fitting result of EPIC 247529791. The atmospheric parameters fitted from these spectra are different from the parameters from the SB2 spectra, too. The best fitting parameters of Figure B.2 are: $T_{\text{eff}1} = 6905.15$ K, $\log g_1 = 3.60$ dex for the primary star, $T_{\text{eff}2} = 6367.69$ K, $\log g_2 = 3.32$ dex for the secondary star, and $[M/H] = -0.31$ dex for the binary system. But the mean parameters of the SB2 spectral fitting are: $T_{\text{eff}1} = 6969.73 \pm 16.30$ K, $\log g_1 = 3.56 \pm 0.06$ dex for the primary star, $T_{\text{eff}2} = 6146.84 \pm 38.50$ K, $\log g_2 = 3.39 \pm 0.30$ dex for the secondary star, and $[M/H] = -0.46 \pm 0.02$ dex for the binary system (Table 4). We don't use the parameters of the near-eclipsing spectra to calculate the final parameters in this work, but we note that our method has the ability to deal with the line-asymmetry spectra with more precise orbital parameters and high S/N spectra.

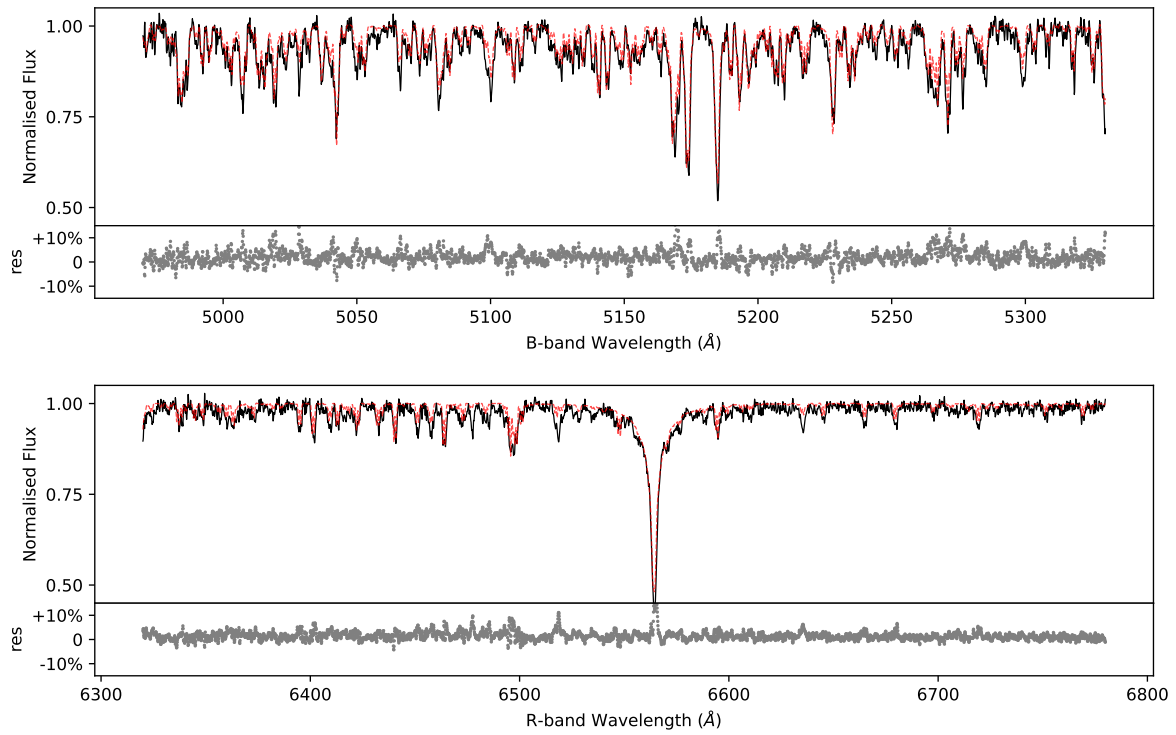


Fig. B.1. The best-fitting result of TIC 63209649 at the near-eclipsing phase. Lines and colours have the same meaning as in Figure 12. This spectrum is also the fifth from the top in Figure 9. The orbital phase of this spectrum is 0.9931.

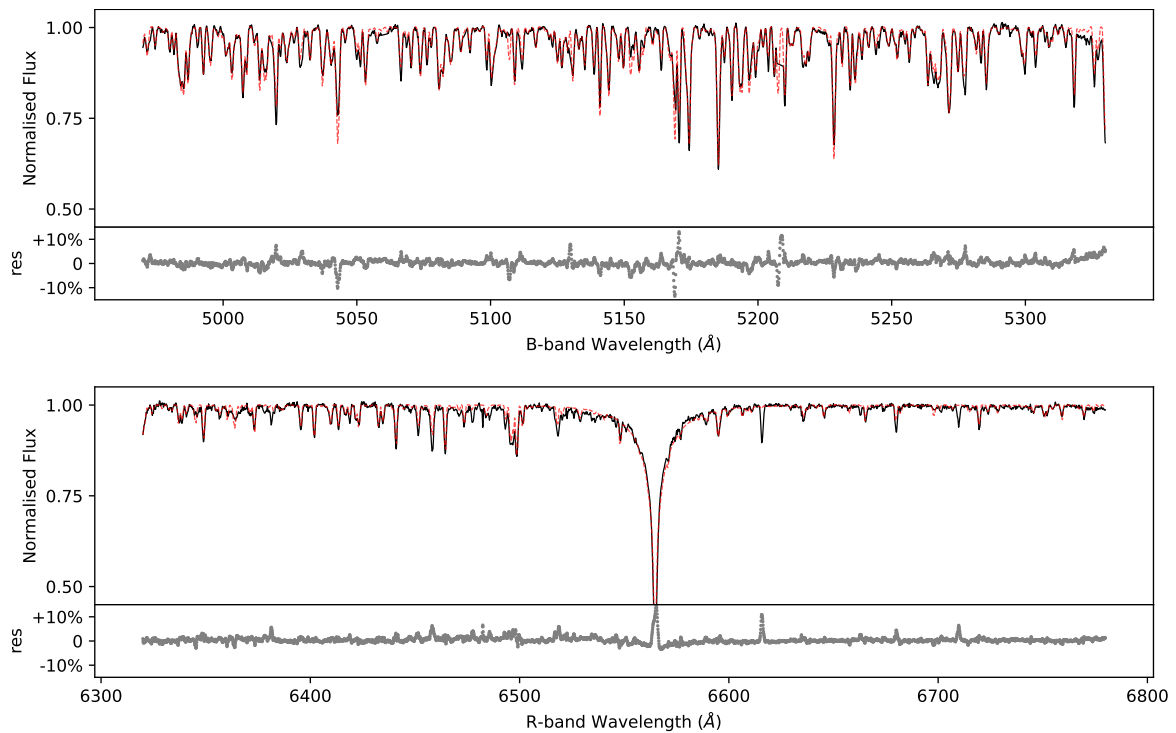


Fig. B.2. The best-fitting result of EPIC 247529791 at the near-eclipsing phase. Lines and colours have the same meaning as in Figure B.1. This spectrum is also the fourth from the top in Figure 15. The orbital phase of this spectrum is 0.0260.